Supplement of Atmos. Chem. Phys., 26, 12019–12036, 2026
https://doi.org/10.5194/acp-26-12019-2026-supplement

Atmospheric Chemistry and Physics
Open Access
EGU

Supplement of

Radiocarbon in atmospheric CH_4 and CO_2 at Jungfraujoch in 2019–2024: influence of regional nuclear emissions and current global atmospheric $^{14}CH_4$ signal

Thomas Laemmel et al.

Correspondence to: Thomas Laemmel (thom.laemmel@gmail.com) and Sönke Szidat (soenke.szidat@unibe.ch)

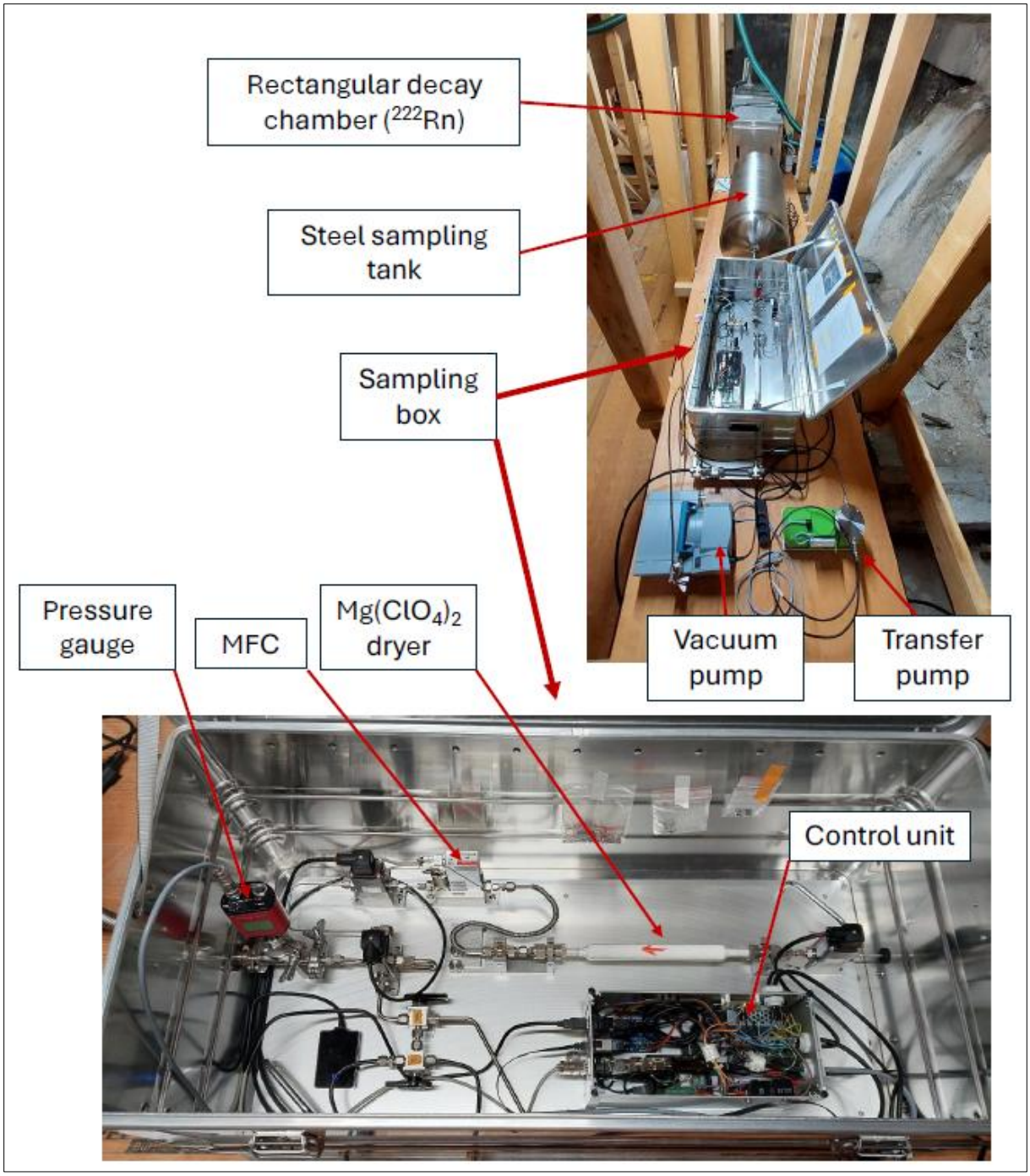

Figure S1: (Top right) picture showing the main components forming the novel integrative sampling installed at Jungfraujoch (JASS) in April 2023. In the background of the picture, the rectangular decay chamber to measure ^{222}Rn is visible. (Bottom) Picture showing the interior of the electronic sampling box.

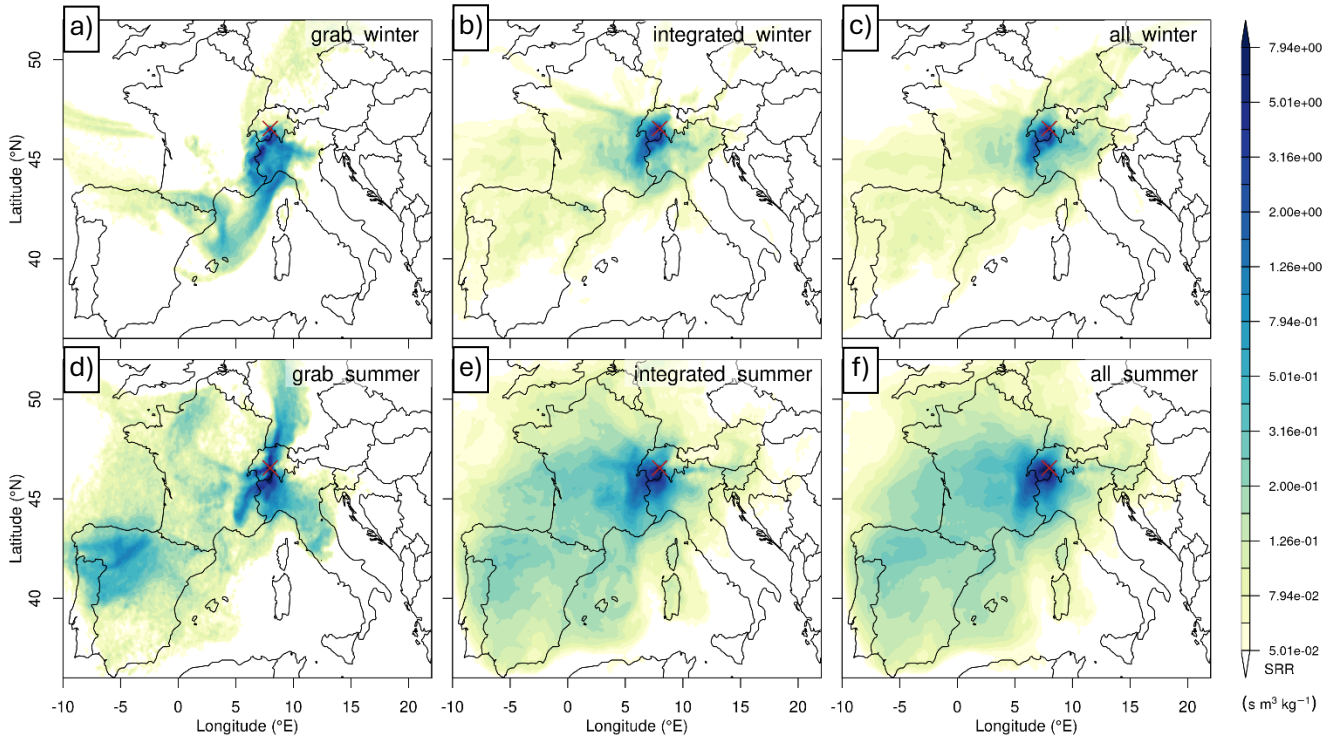

Figure S2: Mean concentration footprints (source-receptor relationships, SRR) calculated with FLEXPART-COSMO for the sampling location Jungfraujoch (red cross) for different sampling strategies (fortnightly grab sampling: a, d; integrated nighttime sampling: b, e; continuous sampling: c, f) and periods (winter: a, b, c; summer: d, e, f) in 2023/2024. Winter: December, January, February; Summer: June, July, August. Grab sampling results in probing specific transport situations, which can be seen by relatively sharp structures in the mean footprint in both summer and winter (a, d). In comparison, integrated night-time sampling (as implemented with the JASS system) results in a much smoother footprint, which is less sensitive to specific transport situations, and, hence, results in a more representative air mass sampling. In line with previous findings (e.g., Herrmann et al. (2015)), concentration footprints are larger during the summer than during the winter as the high-altitude site is more decoupled from lower altitudes in the latter. In addition, continuous sampling in summer leads to a more intense concentration footprint especially close to the site (Switzerland), confirming that nighttime sampling is more suited for deriving baseline conditions.

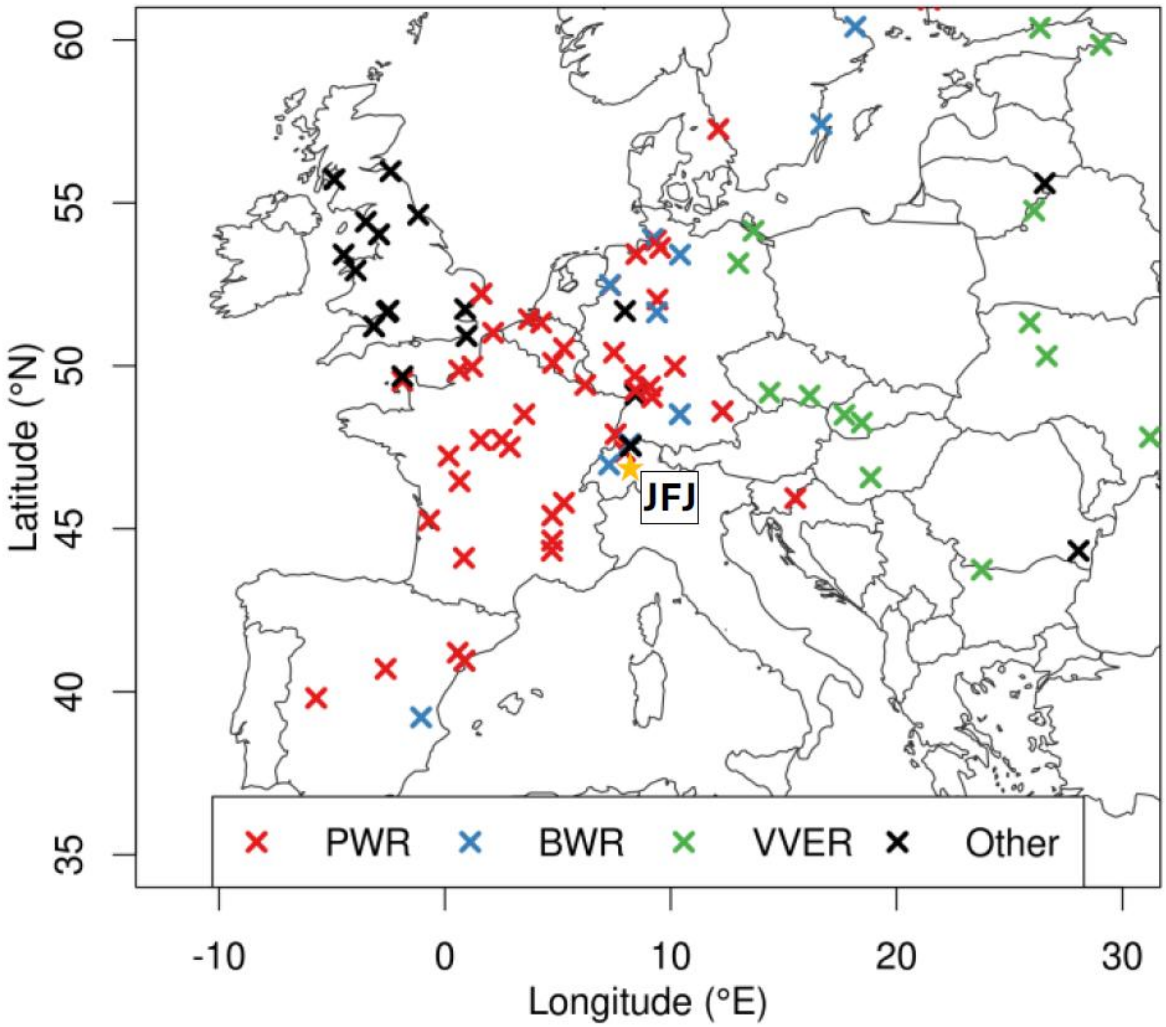

Figure S3: Geographical area (Europe-centered) considered to estimate the $\Delta^{14}C$ nuclear influence on $\Delta^{14}CH_4$ and $\Delta^{14}CO_2$ measurements conducted at Jungfraujoch (orange star). Each cross represents a nuclear power plant considered in the study: a red cross refers to PWRs, a blue cross to BWRs, a green cross to VVERs and a black cross to other reactor types.

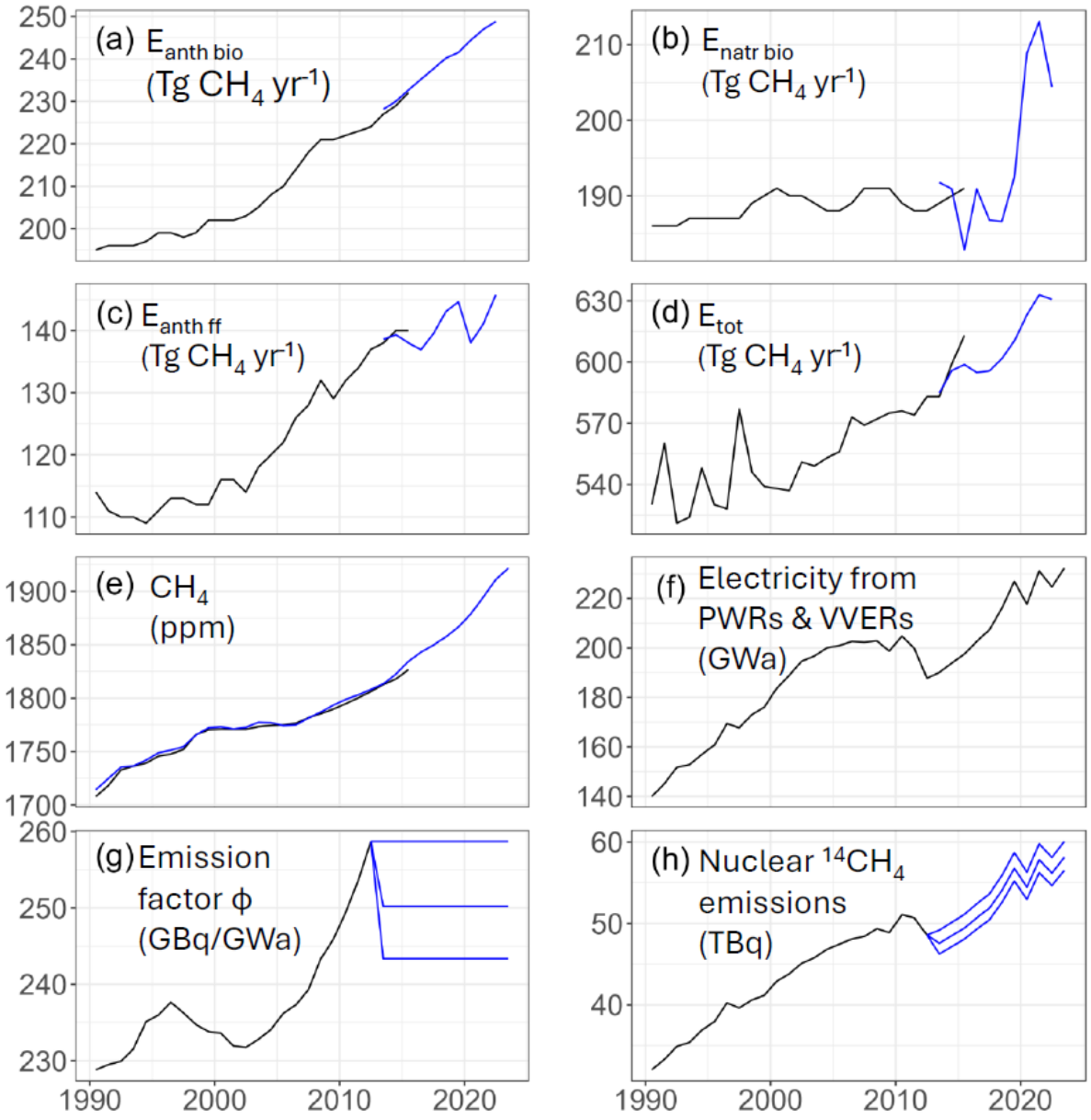

Figure S4: Parameters used to extend the atmospheric one-box model of Fujita et al. (2025) after 2013 (see section 2.6): (a) global anthropogenic biogenic CH_4 emissions $E_{anth\ bio}$, (b) global natural biogenic CH_4 emissions $E_{natr\ bio}$, (c) global anthropogenic fossil fuel CH_4 emissions $E_{anth\ ff}$, (d) global total CH_4 emissions, (e) global atmospheric CH_4 molar fraction, (f) nuclear electricity produced by PWR and VVER reactors according to the inventory by Laemmel and Szidat (2025), (g) emission factor Φ and the three Φ scenarii used for extrapolation after 2013 (in blue), and (h) annual nuclear $^{14}CH_4$ emissions and the three corresponding extrapolations based on previous Φ values (in blue). Black lines in subplots (a), (b), (c) (d), (e), (g) and (h) are derived from Fujita et al. (2025); corresponding blue lines are updated values used in the present study.

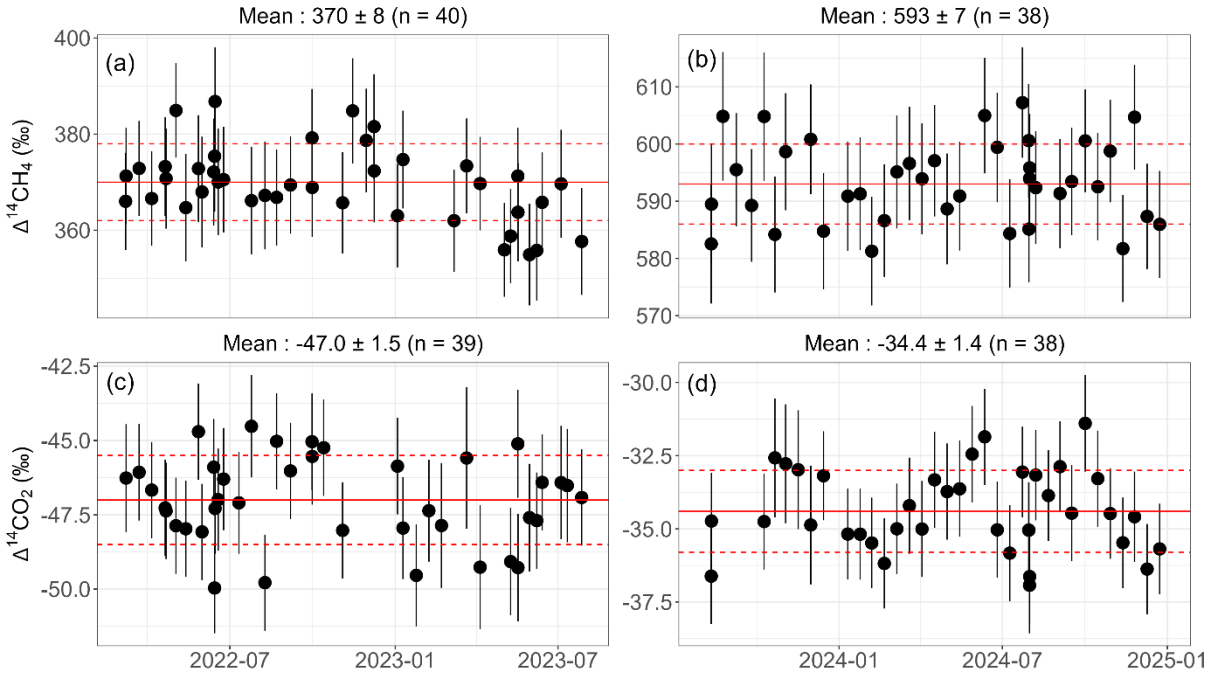

Figure S5: continuous $\Delta^{14}CH_4$ and $\Delta^{14}CO_2$ measurements of the two pressurized air bottles (PAB) (first one from March 2022 to July 2023, second one since August 2023) used as internal standard bottles to evaluate the temporal consistency of our measurements. The red continuous line represents the average value of all the measurements and both dotted lines show the uncertainty range (± standard deviation).

Calculation of $\Delta^{14}C^{Nuc}$ (Section 2.4)

Finally, the annual, quarterly or monthly emission amount of $^{14}CO_2$ and $^{14}CH_4$ available for each plant was equally divided into three-hour intervals to compute an emission rate per output step of the FLEXPART transport simulation:

$$E_i = \frac{A_i \mu_i}{N_A} \frac{t_{1/2,14C}}{ln(2)} \qquad \text{Eq. (S1)}$$

where:

E_i is the mass emission of the radiocarbon element of interest (i = $^{14}CO_2$ or $^{14}CH_4$) (in g s^{-1}),

A_i the radiocarbon emission (i = $^{14}CO_2$ or $^{14}CH_4$) in activity units (Bq),

μ_i the molecular mass of the emitted radiocarbon element (46 g mol^{-1} for $^{14}CO_2$, and 18 g mol^{-1} for $^{14}CH_4$),

N_A the Avogadro constant (6.022 x 10^{23} mol^{-1}),

$t_{1/2,14C}$ the half-life time of radiocarbon (1.799 x 10^{11} s or 5700 years).

FLEXPART-COSMO calculates gridded source sensitivities, τ, in units (g g^{-1}) (s m^3 g^{-1}) (Seibert and Frank, 2004). Multiplication of the source sensitivity of the grid cell containing the nuclear power plant and dividing by the grid box volume, V, yields the radiocarbon mass mixing ratio at the receptor and can readily be converted to the dry-air $^{14}C_i$ mole fraction (i = $^{14}CO_2$ or $^{14}CH_4$):

$$^{14}C_i = E_i \frac{\tau}{V} \frac{\mu_{air}}{\mu_i} \qquad \text{Eq. (S2)}$$

Assuming a mass balance model for $^{14}C_i$ and the mole fraction of all the isotopes of corresponding element (i.e. CO_2 or CH_4) (Graven et al., 2019), a nuclear correction $\Delta^{14}C^{Nuc}$ can finally be derived:

$$\Delta^{14}C^{Nuc} = \frac{\Delta_n^i \, ^{14}C_i}{C_{Obs}} \qquad \text{Eq. (S3)}$$

where Δ_n^i is the $\Delta^{14}C$ signature that a pure ^{14}C sample *i* would have. For a pure $^{14}CO_2$ sample, following (Levin et al., 2010), we used an estimate of Δ_n^{CO2} of 8.21 x 10^{14} ‰, assuming a constant $\delta^{13}C$ value of -8‰. For a pure $^{14}CH_4$ sample, based on a similar calculation, we used an estimate of Δ_n^{CH4} of 8.89 x 10^{14} ‰, assuming a constant $\delta^{13}C$ value of -48‰. C_{obs} represents the mole fraction of the corresponding element i at the receptor; in this study, we used the ICOS measurements at JFJ.

References

Fujita, R., Graven, H., Zazzeri, G., Hmiel, B., Petrenko, V. V., Smith, A. M., Michel, S. E., and Morimoto, S.: Global fossil methane emissions constrained by multi-isotopic atmospheric methane histories, JGR-Atmospheres, https://doi.org/10.1029/2024JD041266, 2025.

Graven, H., Hocking, T., and Zazzeri, G.: Detection of Fossil and Biogenic Methane at Regional Scales Using Atmospheric Radiocarbon, Earth's Future, 7, 283–299, https://doi.org/10.1029/2018EF001064, 2019.

Herrmann, E., Weingartner, E., Henne, S., Vuilleumier, L., Bukowiecki, N., Steinbacher, M., Conen, F., Collaud Coen, M., Hammer, E., Jurányi, Z., Baltensperger, U., and Gysel, M.: Analysis of long-term aerosol size distribution data from Jungfraujoch with emphasis on free tropospheric conditions, cloud influence, and air mass transport, JGR Atmospheres, 120, 9459–9480, https://doi.org/10.1002/2015JD023660, 2015.

Laemmel, T. and Szidat, S.: Compilation of annual nuclear electricity production per reactor from 1954 to 2023, https://doi.org/10.5281/ZENODO.14535156, 2025.

Levin, I., Naegler, T., Kromer, B., Diehl, M., Francey, R. J., Gomez-Pelaez, A. J., Steele, L. P., Wagenbach, D., Weller, R., and Worthy, D. E.: Observations and modelling of the global distribution and long-term trend of atmospheric $^{14}CO_2$, Tellus B: Chemical and Physical Meteorology, 62, 26, https://doi.org/10.1111/j.1600-0889.2009.00446.x, 2010.

Seibert, P. and Frank, A.: Source-receptor matrix calculation with a Lagrangian particle dispersion model in backward mode, Atmos. Chem. Phys., 4, 51–63, https://doi.org/10.5194/acp-4-51-2004, 2004.